ACS Catalysis

Research Article

Cite This: ACS Catal. 2018, 8, 122−131

pubs.acs.org/acscatalysis

Au Nanorod Photosensitized $La_2Ti_2O_7$ Nanosteps: Successive Surface Heterojunctions Boosting Visible to Near-Infrared Photocatalytic H_2 Evolution

Xiaoyan Cai,[†,‡] Mingshan Zhu,[‡] Ossama A. Elbanna,[‡] Mamoru Fujitsuka,[‡] Sooyeon Kim,[‡] Liang Mao,[†] Junying Zhang,*[,†] and Tetsuro Majima*[,‡]

[†]Key Laboratory of Micro-nano Measurement, Manipulation and Physics (Ministry of Education), Department of Physics, Beihang University, Beijing 100191, P. R. China

[‡]The Institute of Scientific and Industrial Research (SANKEN), Osaka University, Mihogaoka 8-1, Ibaraki, Osaka 567-0047, Japan

Supporting Information

ABSTRACT: Visible and near-infrared (NIR) light utilization is a high-priority target for solar-to-chemical energy conversion. In this work, a promising surface heterojunction-based plasmonic photocatalyst was developed by integrating Au nanorods (NRs) with $La_2Ti_2O_7$ nanosteps (Au-LTO NSP) for photocatalytic H_2 evolution in visible and near-infrared (NIR) regions. At wavelengths longer than 420 nm, Au-LTO NSP displayed H_2 production rate that was separately 2.4 and 4.7 times that of Au-LTO nanosheets (NS) and Au−P25 composites, using methanol as the sacrificial agent. At wavelengths longer than 780 nm, the enhancement was 2.3 and 5.8 times, respectively. The high apparent quantum efficiency (AEQ) of 1.4% at 920 nm irradiation makes the Au-LTO NSP photocatalyst especially efficient for the NIR light utilization. The broadband photocatalytic activity of Au-LTO NSP was mainly caused by longitudinal surface plasmon resonance of Au NRs, generating and injecting hot electrons into LTO NSP. Substantial electrons transferred from Au NRs to the (010) facets and then directionally migrated to the (012) facets of LTO NSP, as consequence of the successive (010) and (012) surface heterojunctions within a LTO NSP single particle. The unique step structure of LTO retarded the recombination of the photoinduced electrons and holes in Au NRs, showing the powerful role of the semiconductor surface heterojunction in favoring the plasmon-induced interfacial hot electron transfer.

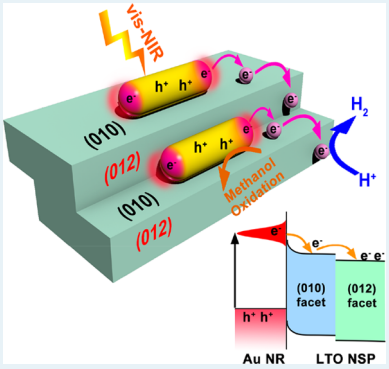

KEYWORDS: *plasmonic photocatalysis, vis−NIR light, surface heterojunction, hot electron transfer*

INTRODUCTION

Hydrogen (H_2) has been known as an ideal source of energy due to its environmental friendliness and high energy capacity.[1] Since the pioneering work on photoelectrocatalytic splitting of water by TiO_2 under UV light irradiation,[2] H_2 evolution via photocatalytic water splitting has been extensively studied and shown to be a promising solution for alleviating worldwide energy issues.[3−5] TiO_2 is the most common semiconductor photocatalyst used for solar H_2 generation.[6] However, because of the large band gap of TiO_2, its light harvesting is limited in UV light region which only accounts for ca. 4% of the solar spectrum.[5] Fully harvesting solar light, from the visible to near-infrared (NIR) region, is always the goal and challenge for photocatalysis.[7] Unfortunately, only a few semiconductors reveal NIR activity. Because of the low photon energy or strong thermal effect, narrow bandgap semiconductors with NIR light absorption usually either lack photocatalytic activity or convert NIR light energy into heat directly.[8] For example, black hydrogenated TiO_2 revealed significantly broadened absorption in the vis−NIR region, but only ca. 1% enhancement of the photocatalytic activity has been achieved.[9−11] Up-conversion materials were used by many researchers to convert NIR light into visible and UV light.[12−14] For instance, NIR photocatalytic degradation of organic dyes was achieved by Yb^{3+} and Tm^{3+} codoped mesoporous TiO_2, but the overall conversion efficiency was significantly low since a 980 nm laser had to be used.[12] Recently, the surface plasmon resonance (SPR) effect has been exploited to realize photocatalytic splitting of water in the NIR region.[15−20] Depending sensitively on the nanostructure of the metal and the dielectric properties of the surrounding environment, the SPR bands of the plasmonic metal are tunable from UV to NIR.[15] When a plasmonic metal is coupled to a semiconductor, the plasmon energy can transfer from the metal to the semiconductor, enhancing charge generation via hot electron/hole transfer, photonic enhancement, and local electromagnetic field enhancement.[16,21,22] In addition, by forming Schottky barriers, the recombination of photoexcited electron−holes can be significantly reduced. For example, Au nanorods (NRs)/CdS composite photocatalysts were fabricated to generate H_2 under

Received: August 31, 2017
Revised: November 2, 2017
Published: November 21, 2017

DOI: 10.1021/acscatal.7b02972
ACS Catal. 2018, 8, 122−131

vis−NIR light irradiation.[23] By tuning the ratio of length and width, the optical resonance of Au NRs covers most of the solar spectrum, which can be used to design panchromatic absorbers. Accordingly, Au NRs decorated semiconductors have offered a new opportunity to achieve more efficient utilization of the solar spectrum.

The geometry and location of the plasmonic metallic nanostructures relative to the neighboring semiconductors, as one of the most crucial factors for efficient hot electron transfer from plasmonic nanostructures to semiconductor materials, have been intensively studied.[24−28] Recently, Majima's group found that a large part of electrons could transfer from Au nanospheres to TiO_2 with coexposed {001} and {101} facets while only a few electrons to TiO_2 nanoparticles through SPR excitation using the time-resolved diffuse reflectance spectroscopy.[29] The electron transport dynamics from plasmonic metal to the neighboring semiconductor are also greatly influenced by the geometry (morphology, structure, and exposed crystal surface) of the semiconductor.[30−32] Particularly, plasmon-induced chemical reactions of Au nanostructures loaded on semiconductor substrates with coexposed different crystal surfaces have attracted growing attention in photocatalysis, because the directional migration of hot electrons in the semiconductor can be facilitated by taking advantage of the Schottky barrier between the Au nanostructure and the crystal surface of the semiconductor.[29,33] However, to the best of our knowledge, few papers deal with optimizing the exposed crystal surface of the semiconductor to efficiently achieve Au NR induced broad spectrum photocatalytic H_2 evolution.

Herein, we propose a new design for the efficient utilization of a broad spectrum from visible to NIR light toward enhanced plasmonic photocatalytic activity in H_2 evolution. Au NRs with visible and NIR plasmonic absorption were decorated on the surface of $La_2Ti_2O_7$ nanosteps (Au-LTO NSP), which have been demonstrated to exhibit higher electron flow and remarkably long-lived charges compared to nanoparticles (NP) and nanosheets (NS) because of the successive surface heterojunctions.[34] The photocatalytic H_2 generation performance of the Au-LTO NSP composite was significantly higher than that of Au-LTO NS and Au−P25, under wavelengths longer than 420 and 780 nm light irradiation. Especially, the Au-LTO NSP composite performs well in the NIR region, promising the more efficient utilization of the long-wavelength solar light in comparison with similar materials. Single-particle photoluminescence (PL) spectroscopy and femtosecond time-resolved transient absorption measurements provided direct evidence that the plasmon-induced interfacial hot electrons transfer from Au NRs to LTO nanostructures. The effect of the successive surface heterojunctions of LTO NSP on the interfacial hot electron transfer dynamics was fully investigated.

RESULTS AND DISCUSSION

Morphology, Structure, and Optical Properties. The synthesis procedures of Au NRs decorated LTO nanosteps (Au-LTO NSP) composites by a facile self-assembly approach are schematically shown in Figure 1a. Typically, Au NRs samples with a longitudinal surface plasmon resonance (LSPR) absorption peak located at 780, 860, and 940 nm (Figure S1a) were prepared through seed-mediated strategy and then attached on the mercaptopropionic acid (MPA)-functionalized LTO nanostructures by ligand exchange for the construction of Au-LTO composites. The intermediate ligand of MPA can replace the original capping agent CTAB on Au NRs,

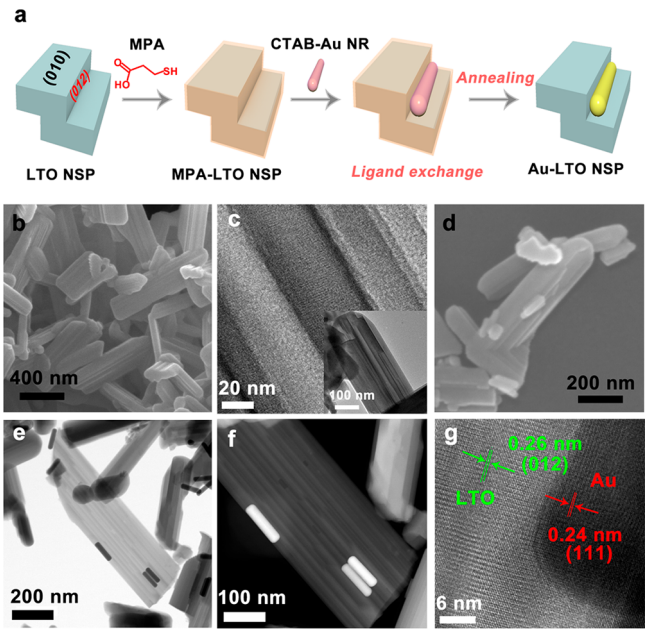

Figure 1. Schematic illustration of the preparation for Au-LTO NSP composites (a). SEM (b) and TEM (c) images of LTO NSP. SEM (d), TEM (e, f), and HRTEM (g) images of Au-LTO NSP.

facilitating a strong interaction between Au and LTO through its thiol and carboxylic groups, respectively.[35] The samples are denoted as 780-, 860-, and 940-Au-LTO NSP, respectively, based on the absorption maximum. Scanning electron microscopy (SEM) and transmission electron microscopy (TEM) images were taken to analyze the morphology of the samples. As seen from Figure S1b-d and Table S1, Au NRs in three samples exhibit different aspect ratios, leading to the different light harvesting ability (Figure S1a). Figure 1b shows a SEM image of three-dimensional (3D) LTO crystals in a polygonal cross profile with about 100−500 nm size obtained through a molten-salt growth process. The uniform strip-like structures on the surface of LTO particles are the edge/boundary of steps. The TEM image demonstrates that the nanostep is enclosed by several well-defined terraces through internal and external stairways (Figure 1c). The LTO NSP are single-crystalline and grow by stacking well-organized multilayers along the direction of [010], with periodically coexposed high-energy (012) facets and low-energy (010) facets as explained in our previous work.[34] Under high temperature (1100 °C) condition, the formation energy of (010) surfaces is increased while that of the (012) surface decreased because the molten salt ions (Na^+ or Cl^-) enriched in (012) surfaces to prevent the crystal growth along the [012] direction, inducing the exposure of (012) facets and thus the formation of the step structure. With regard to 860-Au-LTO NSP composites, it can be observed from Figure 1d−f that the Au NRs are well loaded on the step-structured LTO surfaces by the effective 1D/3D interfacial interaction. The high resolution TEM (HRTEM) image of the interface of LTO and Au regions shows the identified lattice spacing of 0.26 and 0.24 nm, corresponding to the (012) facet of the monoclinic phase LTO and the (111) crystal plane of the cubic phase Au, respectively (Figure 1g). Scanning transmission electron microscopy (STEM) and energy dispersive X-ray spectroscopy (EDS) elemental mapping in Figure S2 further confirm the decoration of Au NRs on LTO NSP. The EDS analysis of the whole area of

DOI: 10.1021/acscatal.7b02972
ACS Catal. 2018, 8, 122−131

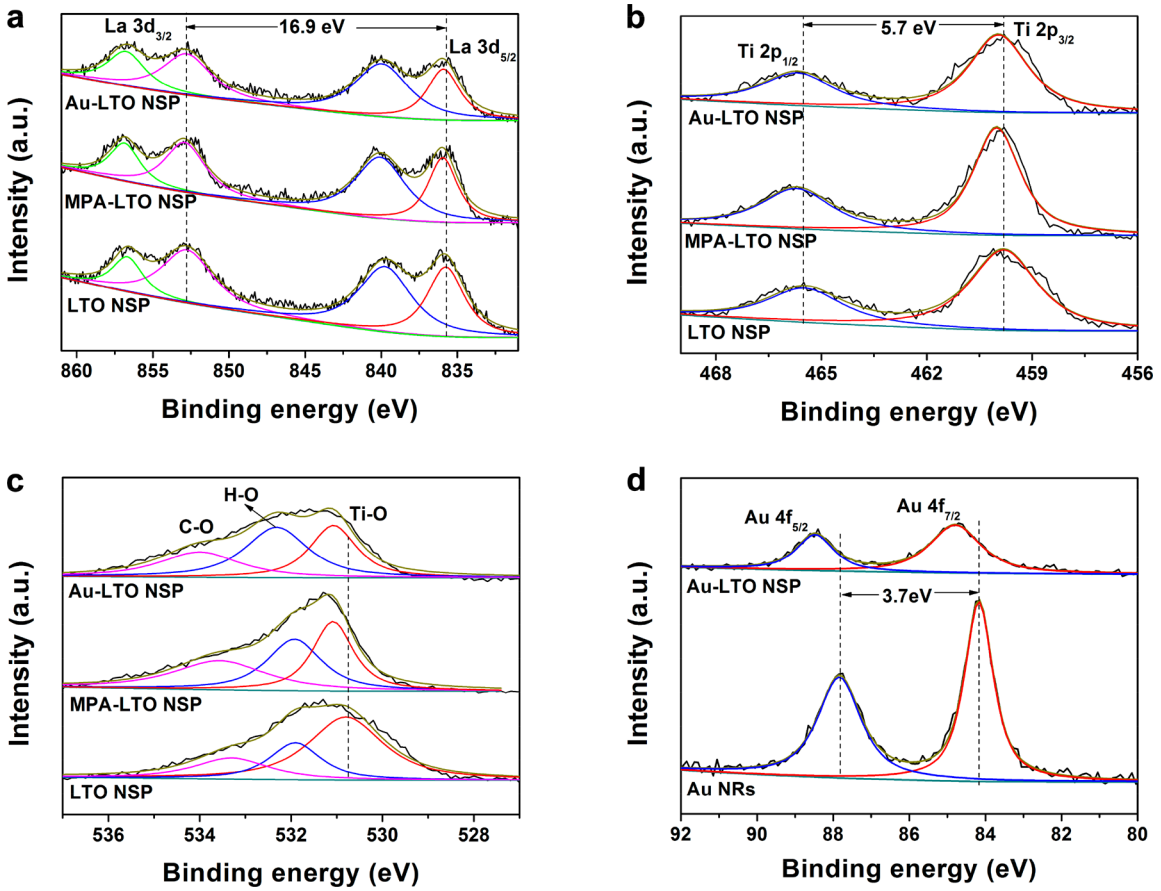

Figure 2. High-resolution XPS of La 3d (a), Ti 2p (b), O 1s (c), and Au 4f (d) in LTO NSP, MPA-LTO NSP, Au-LTO NSP, and Au NRs samples.

Figure 1e showed that weight ratio of La, Ti, O, and Au is 2.5:1.0:0.70:0.13 (Figure S3), indicating that the Au-LTO NSP sample contains about 3 wt % of Au.

The crystal and chemical structures of as-synthesized Au-LTO composites were investigated by X-ray diffraction (XRD). Figure S4 shows the XRD patterns of LTO NSP and 860-Au-LTO NSP decorated with 3 wt % Au NRs. It is clearly seen that both samples exhibit good crystallinity and distinct diffraction peaks corresponding to perovskite structured LTO with the monoclinic crystalline phase (JCPDS no. 70-0903). The LTO phase in Au-LTO NSP composites displays similar diffraction peaks to those of LTO NSP, indicating negligible structural modifications of LTO NSP after its adsorption of Au NRs by the surface functionalized process. The XRD patterns of Au-LTO NSP composites indicate two additional peaks at 38.4° and 44.6°, corresponding to the (111) and (200) crystal planes of cubic Au (JCPDS no. 04-0784), respectively.

To learn in-depth fundamental information on the interaction of Au NRs with LTO NSP, X-ray photoelectron spectroscopy (XPS) of La 3d, Ti 2p, O 1s, and Au 4f of the samples was measured as shown in Figure 2, and their survey spectra are presented in Figure S5. First, La 3d spectra of LTO NSP show doublet peaks at 835.8 and 852.7 eV with good symmetry (Figure 2a), indicating that the La ions are in the oxidation state La^{3+}.[36] Second, the bare LTO sample exhibits symmetric Ti $2p_{3/2}$ and $2p_{1/2}$ peaks at 459.8 and 465.5 eV, respectively (Figure 2b), with a peak separation of 5.7 eV, being in good agreement with the energy splitting reported for TiO_2.[36,37] Third, the O 1s region (Figure 2c) was fitted by three peaks in LTO, in which the Ti−O appeared at 530.8 eV, the physisorption of (OH) and chemisorbed H_2O appeared at 531.7 eV, and the C−O bond appeared at 533.1 eV.[38] As for MPA-LTO NSP and Au-LTO NSP sample, the above assigned peaks (La 3d, Ti 2p, and Ti−O) are positively shifted by 0.2−0.4 eV, as compared to those for LTO NSP. This phenomenon can be explained by the surficial interaction of the MPA ligand with LTO NSP. For Au 4f spectra, as shown in Figure 2d, around 3.7 eV of peak separation between Au $4f_{7/2}$ (84.1 eV) and Au $4f_{5/2}$ (87.8 eV) was observed, indicating the formation of metallic Au.[36] Similarly, when Au was attached on LTO, the signals of Au 4f shift to higher binding energies (ca. 0.7 eV), suggesting a strong interaction between Au and LTO in the Au-LTO system.[38]

The diffuse reflectance spectra (DRS) of LTO NSP and Au-LTO NSP were recorded in the range of 200−1200 nm, as shown in Figure 3. The bare LTO NSP can absorb only UV light with wavelengths λ < 383 nm due to the bandgap energy (3.23 eV). After loading Au NRs, the optical absorption thresholds of 780-, 860-, and 940-Au-LTO NSP are all similar to those of bare LTO NSP. However, two additional absorption bands centered at visible and NIR regions appear, as a consequence of the transverse surface plasmon resonance (TSPR) and LSPR photoabsorption of Au NRs, respectively. As we know, the SPR absorption band is sensitive to the surrounding environment of the metal nanostructure.[15] Compared to bare Au NRs colloids (Figure S1a), both TSPR and LSPR absorptions of the corresponding Au-LTO NSP samples are red-shifted due to the large refractive index of the semiconductor substrate.[39] By comparing the spectra of Au-LTO NSP samples, it is found that the aspect ratio of Au NRs

DOI: 10.1021/acscatal.7b02972
ACS Catal. 2018, 8, 122−131

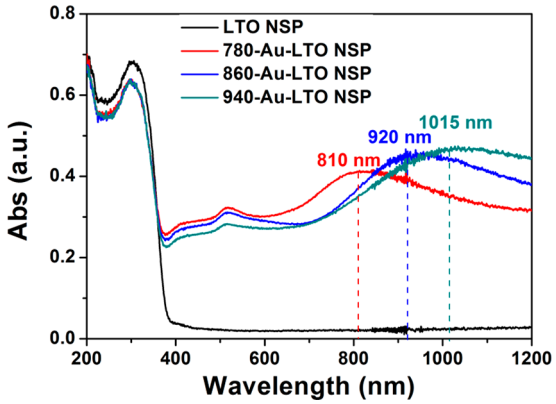

Figure 3. UV−vis−NIR DRS of LTO NSP and Au-LTO NSP samples.

has a great influence on the plasmon absorption of the composites. The maximum LSPR absorption of Au-LTO NSP shifts to low resonance energy with the increase of the aspect ratio of Au NRs. These results show that the light harvesting properties of Au-LTO NSP composites can be flexibly adjusted by changing the aspect ratio of Au NRs. Furthermore, the board absorption peak in the NIR region offers a new opportunity for the utilization of a long-wavelength solar spectrum.

Photocatalytic H_2 Evolution Activities. To understand the plasmonic effect of Au NRs on promoting photocatalysis, the testing of Au-LTO systems in reductive generation of H_2 was performed under vis−NIR light ($\lambda > 420$ nm) or NIR light ($\lambda > 780$ nm) irradiation, by putting a 420 or 780 nm long-pass filter between the reactor and light source (a Xe lamp with output wavelength, 350−1800 nm, 350 mW cm^{-2}). Under such conditions, the bandgap photoexcitation of LTO can be prevented so that the SPR-mediated local electromagnetic field enhancement and photonic enhancement mechanism cannot work in our systems, and thus the SPR excitation effects of Au NRs in the composites are exclusively studied.[40] The H_2 evolution amount obtained in our experiments corresponded to three times of independent tests using three samples prepared independently, wherein methanol was used as a sacrificial electron donor. Figure 4a shows the H_2 evolved over 780-, 860-, and 940-Au-LTO NSP samples with equivalent Au NRs loadings (3 wt %) under the $\lambda > 420$ nm light irradiation. The amount of H_2 generated from the 780-, 860-, and 940-Au-LTO NSP composites increased with time and reached 0.83 ± 0.08, 1.07 ± 0.09, and 0.92 ± 0.04 mmol g^{-1} under vis−NIR light irradiation for 3 h, respectively. Among the tested samples, 860-Au-LTO NSP exhibits the highest photocatalytic activity, which may be induced by the higher light intensity of Xe lamp in the NIR region ranging from 800 to 900 nm (Figure S6). As the irradiated wavelength was longer than 780 nm, similar phenomena were observed (Figure S7), demonstrating that Au NRs are suitable photosensitizers under both visible and NIR light irradiation. As a reference experiment, LTO NSP exhibited no obvious photocatalytic activity because the low energy photons coming from a filtered Xe lamp cannot cause

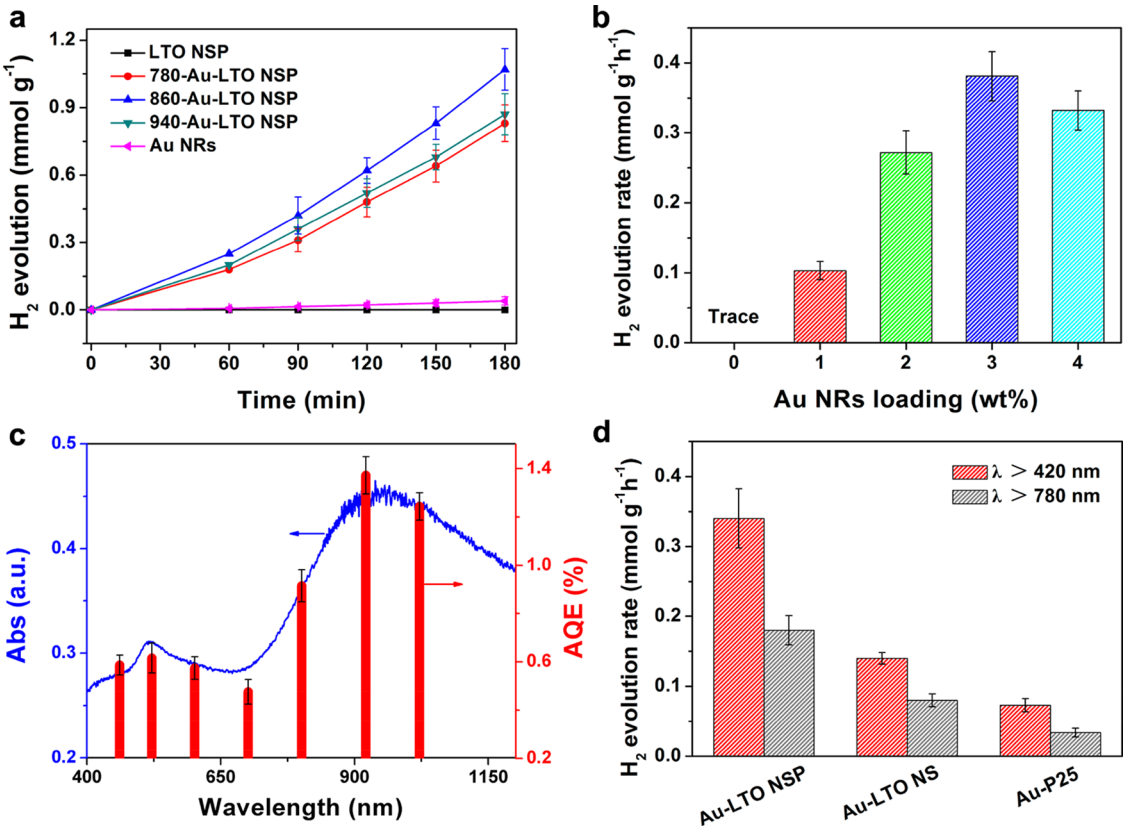

Figure 4. Photocatalytic H_2 evolution over different samples with 3 wt % Au loading (a) and effect of Au loading amounts in Au-LTO NSP on photocatalytic H_2 evolution rate (b) under vis−NIR ($\lambda > 420$ nm) light irradiation. DRS (left axis, blue line) and AQE (right axis, red column) of Au-LTO NSP (c). Photocatalytic H_2 evolution rate over different samples with 3 wt % Au loading under vis−NIR ($\lambda > 420$ nm) and NIR ($\lambda > 780$ nm) light irradiation (d).

DOI: 10.1021/acscatal.7b02972
ACS Catal. 2018, 8, 122−131

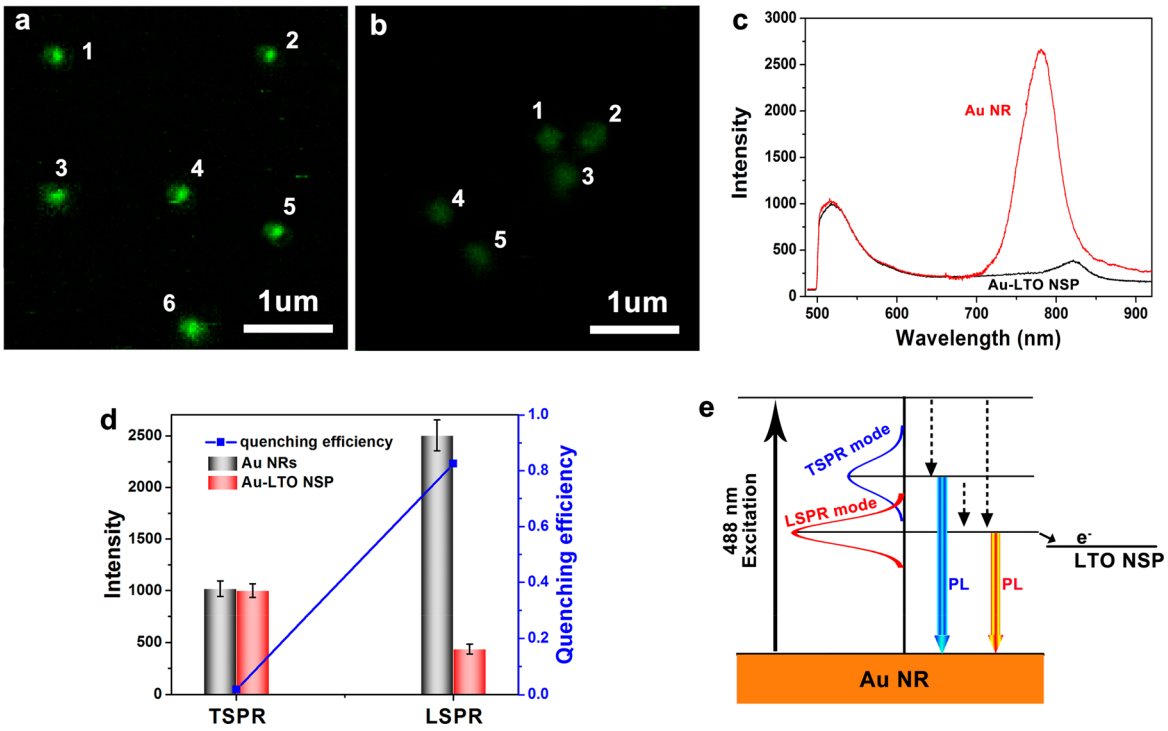

Figure 5. Single-particle PL images of Au NRs before (a) and after (b) loading on LTO NSP. Typical single-particle PL spectra of Au NRs before and after loading on LTO NSP (c). Averaged intensity (left axis, column) and quenching efficiency (right axis, line+symbol) of single-particle PL spectra of Au NRs loaded on LTO NSP (d). SPR radiative decay of hot electron on Au NR loaded on LTO NSP (e).

the bandgap photoexcitation of LTO. Moreover, negligible H_2 generation was observed with Au NRs alone since the energetically hot electrons cannot be effectively extracted and migrated to participate in photocatalytic processes although Au NRs have significant SPR absorption.[23] These results indicate that the interaction between Au and LTO plays a crucial role in the photocatalytic H_2 evolution. Figure 4b summarizes the effects of the loading amount of Au NRs on the photocatalytic activity of 860-Au-LTO NSP nanocomposites under light illumination with wavelengths longer than 420 nm. The photocatalytic H_2 generation performance initially increases and eventually decreases when the loading amount of the Au NRs increases. The optimal amount of Au NRs in the present photocatalytic system is demonstrated to be 3 wt %, which led to a H_2 evolution rate of 0.34 ± 0.03 mmol g^{-1} h^{-1}. The decrease in the photocatalytic activity can be attributed to the increased recombination events of the photoelectrons and holes as a result of the high number density of the Au NRs, since Au particles can dually serve as recombination centers for photoinduced electrons and holes.[41] The photocatalytic stability of Au-LTO NSP was investigated by cyclic photocatalytic H_2 evolution experiments. As shown in Figure S8, continuous H_2 evolution was detected without noticeable degradation in the subsequent runs. No obvious change could be observed in the XRD pattern and SEM and TEM images of Au-LTO NSP after the photocatalytic reaction (Figure S9), indicating that the Au NR decorated LTO NSPs act as stable photocatalysts.

To verify whether the vis−NIR light responsive activity came from the SPR excitation of Au NRs, we measured the H_2 evolved over 860-Au-LTO NSP at a series of monochromatic light (width: ±5 nm; intensity: ∼10 mW cm^{-2}). The calculated apparent quantum efficiency (AQE) at each wavelength was averaged by three repeated tests. From Figure 4c, one can see that the AQE action spectrum basically agrees with the SPR spectrum of the 860-Au-LTO NSP composite. Especially, the AEQ of 1.4 ± 0.1% at 920 nm indicates that the Au-LTO NSP composites perform well in the NIR region. The result implied that the observed H_2 evolution was originated from the LSPR rather than TSPR excitation of Au NRs, which will be further confirmed by single-particle PL measurements below.

In order to investigate the impact of the LTO structure on the SPR-mediated system, we prepared two reference samples, Au-LTO NS and Au-P25, containing the same amount of 860-Au NRs as Au-LTO NSP. Their XRD, TEM, and DRS analyses are displayed in Figures S10 and S11, respectively. Sheet-like LTO exposed with (010) surfaces was obtained through hydrothermal processing (300−800 nm lateral size, 10 nm thickness, and 44 m^2 g^{-1} surface area).[34] Due to the unbounded oxygen atoms, the perovskite LTO is readily formed into a two-dimensional (2D) plate and exposes the O-terminated inactive (010) surfaces. Commercial P25 TiO_2 powder was often used as a benchmark in photocatalysis (particle size: 19 nm; surface area: 55 m^2 g^{-1}).[29] Both LTO NS and P25 TiO_2 have no absorption for visible light and possess a much larger surface area than LTO NSP (5.7 m^2 g^{-1}).[34] After loading Au NRs onto LTO NS, two new absorption bands appear at around 520 and 920 nm (Figure S10c), ascribing to the TSPR and LSPR excitation of Au NRs, respectively. The Au-P25 sample shows the SPR absorption peaks at about 520 and 900 nm, respectively (Figure S11c). The optimal Au NRs loading amounts on LTO NS and P25 were determined to be 3 and 1 wt %, respectively (Figure S12). As summarized in Figure 4d, with 3 wt % Au NRs loading, these two composites exhibited lower activity than Au-LTO NSP, in which the H_2 generation rate (0.34 ± 0.03 mmol g^{-1} h^{-1}) was 2.4 and 4.7 times that of Au-LTO NS (0.14 ± 0.008 mmol g^{-1} h^{-1}) and Au−P25 (0.073 ± 0.009 mmol g^{-1} h^{-1}) under λ > 420 nm light irradiation,

DOI: 10.1021/acscatal.7b02972
ACS Catal. 2018, 8, 122−131

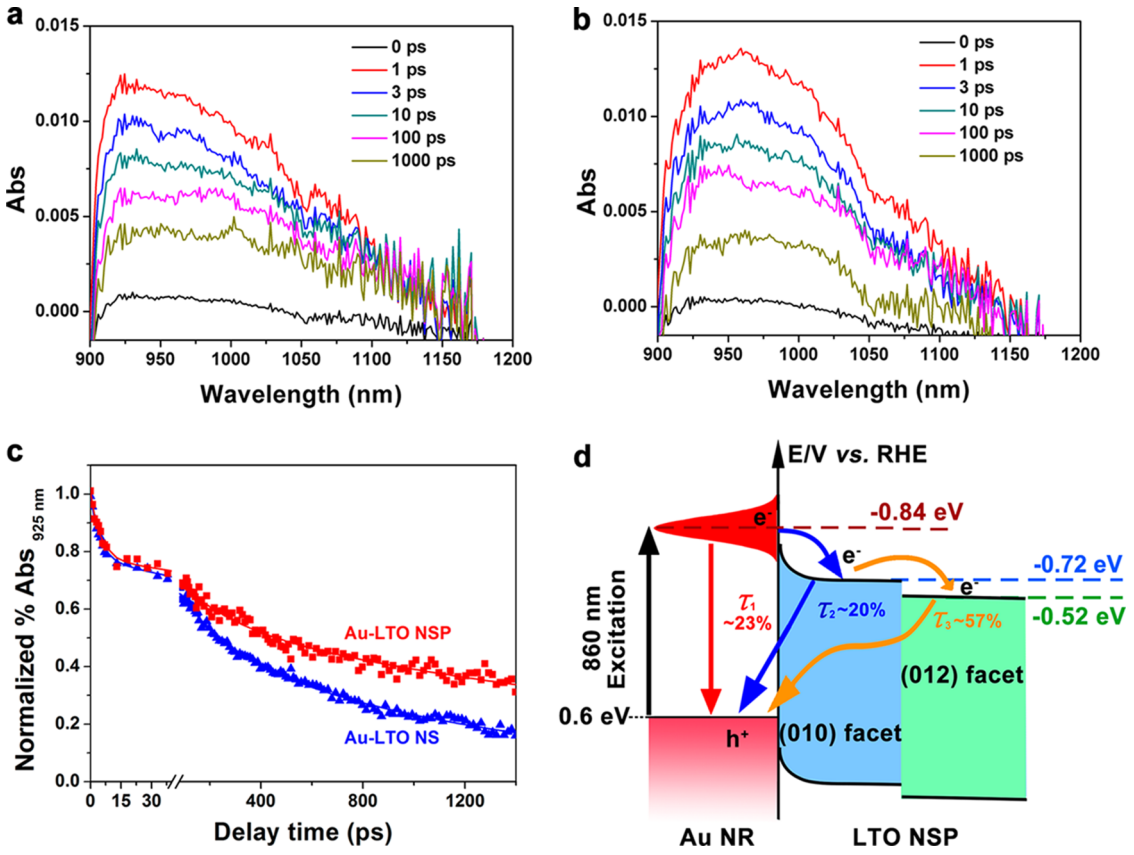

Figure 6. TDR spectra observed after 860 nm laser flash photolysis of Au-LTO NSP (a) and Au-LTO NS (b). Normalized transient absorption traces observed at 925 nm for Au-LTO NSP and Au-LTO NS systems (c). Bold lines indicate multiexponential curves fitted to kinetic traces. Schematic illustration of the three different electron decay processes in the Au-LTO NSP system (d).

respectively. When it comes to NIR light illumination (λ > 780 nm), the photocatalytic H_2 evolution rates of Au-LTO NSP, Au-LTO NS, and Au-P25 were measured to be 0.18 ± 0.02, 0.080 ± 0.009, and 0.031 ± 0.006 mmol g^{-1} h^{-1}, respectively (Figure 4d). The poor activity of the Au-P25 composite may be induced by the insufficient interfacial contact between Au NRs and P25 nanoparticles. The above results indicated that the step-like LTO nanostructure is a superior electron acceptor when SPR Au NR is used as a hot electron donor. Photocurrent and electrochemical impedance spectra (EIS) of the three samples were measured as shown in Figure S13, which further demonstrated the higher charge separation in Au-LTO NSP.

Interfacial Hot Electron Transfer Dynamics. Single-particle PL microscopy was used to clarify the spatial electron transfer from single Au NR to LTO NSP. Using a 488 nm CW laser as the excitation light source, PL images and the corresponding spectra were detected by the electron-multiplying charge-coupled device (EMCCD) camera. It is essential to achieve the monodispersibility of nanorods for the statistical PL evolution of Au NRs. A typical SEM image of monodispersed Au NRs on a glass substrate is shown in Figure S14a, confirming the monodispersibility of the sample. Figure 5a shows single-particle PL images of Au NRs, while single-particle PL spectra of the Au NR particles identified by the number in Figure 5a are shown in Figure S15. A strong PL peak at longer wavelength (~800 nm) which can be assigned to PL from LSPR was observed for each particle. Because of the different aspect ratio of individual Au NR particles, the position and intensity of LSPR PL bands have some differences. The presence of a long pass filter (498 nm) installed to remove the excitation light obstructed the full display of the PL at the TSPR region (~520 nm). When Au NRs were loaded on the surface of LTO NSP, the dispersed sample on a glass substrate is also observed by a SEM image in Figure S14b. Compared with bare Au NRs, the brightness of single-particle PL images of Au NRs loaded on LTO NSP became weak because of the PL quenching by LTO (Figure 5b). In the same manner, single-particle PL spectra of the Au NR particles on LTO NSP indexed by the number in Figure 5b are shown in Figure S16. The PL quenching was clearly observed in the spectra in Figure 5c. After analyzing the PL spectra of 30 individual Au NRs with and without LTO adsorption, we can compare the absolute values of the LSPR and TSPR PL intensities (Figure S17). Upon composing with LTO, the PL intensities at the LSPR region substantially decreased while that at the TSPR region remained nearly unvaried. Moreover, the averaged intensity and quenching efficiency of SPR PL bands of the 30 Au NR particles were calculated (Figure 5d). The quenching efficiencies of PL from TSPR and LSPR for Au-LTO NSP were 2% and 82%, respectively, indicating that the hot electrons transfer from Au NRs to LTO was mainly caused by the LSPR of Au NRs.

Under 488 nm laser light irradiation, electron−hole pairs was generated in Au NRs via the interband transition. The short-wavelength PL peak is caused by a fast interconversion occurring between the electron−hole pairs and TSPR which subsequently decay radiatively.[42] The LSPR PL is induced by the directly excited hot electrons which may lose the energy nonradiatively and interconvert to the LSPR mode, emitting a photon subsequently.[42] In the meantime, promoting by

DOI: 10.1021/acscatal.7b02972
ACS Catal. 2018, 8, 122−131

electron−hole pairs, an energy transfer occurs from the TSPR to LSPR mode (Figure 5e).[19] As reported, the PL lifetime from the TSPR mode is much shorter than that from the LSPR mode,[43] implying that some other decay routes are easier to influence the LSPR PL, while the TSPR PL is invariant and more related to its intrinsic features. In this work, PL damping occurred when Au NRs were loaded on LTO, as a result of hot electrons transfer from Au NRs to LTO, competing with the LSPR emission. Under vis−NIR light irradiation, the hot electrons are generated by TSPR/LSPR excitation and then transfer to LTO, where H^+ reduces to H_2. In the visible light region, the AQE of Au-LTO NSP for H_2 evolution was lower than 1% (see Figure 4c). Because TSPR excitation was the dominant hot electrons generation path, the interband energy transition from TSPR to the LSPR mode could only lead to a low quenching efficiency of 2% for TSPR PL upon composing with LTO. In the NIR light region, the dominant LSPR excitation caused abundant hot electron injection (82%) from Au NRs into LTO, giving rise to a very high AQE for H_2 evolution. The electron-transfer process causes charge separation spatially.[19] The spatial separation of plasmon-induced hot electron−hole pairs in Au NRs decorated LTO NSP results in an efficient charge separation and, hence, an improved NIR light utilization for H_2 production.

In our previous publication, successive surface heterojunctions constituted by two periodically arranged facets in nanostep structured LTO were demonstrated to efficiently enhance space-charge separation.[34] Due to different band structures and band edge positions, the periodically coexposed high-energy (012) facets and low-energy (010) facets of LTO NSP can form successive surface heterojunctions within a single LTO particle, which is beneficial for the transfer of photogenerated electrons and holes to (012) and (010) facets, respectively. In the present work, we can conclude that photogenerated hot electrons from Au NRs could migrate to LTO NSP more easily and efficiently than in LTO NS when Au NRs is irradiated under visible and NIR light. However, the electron transfer behavior from Au NRs to LTO with different geometry (morphology, structure, and exposed crystal surface) is still unclear, which is a significant factor influencing the photocatalytic H_2 production activity. Therefore, femtosecond time-resolved diffuse reflectance (TDR) spectroscopy, a powerful analytical tool in understanding fundamental photophysical processes, was carried out here to help us directly observe the dynamics of electron transfer time-scale and carrier populations after the SPR excitation. The TDR spectra of Au-LTO NSP and Au-LTO NS were recorded at different time delays after exciting Au NRs with 860 nm pump pulse laser. The spectra of all samples revealed a broad absorption band from 900 to 1200 nm (Figure 6a,b), which could be assigned to trapped and free (or shallowly trapped) hot electrons generated from the LSPR mode of Au NRs according to the previous studies.[44,45] The transient absorption of all samples reached highest immediately after the laser flash (1 ps) and then decayed gradually, showing a subpicosecond time scale of the electron injection process from the excited Au NRs to LTO. At 1−1000 ps after the laser flash, the concentration of electrons in the Au-LTO composite reduced in a multiexponential decay owing to the recombination of these electrons with the holes in Au NRs.[29] At 1000 ps, approximately 40% of the electrons survived in the Au-LTO NSP system, while only ∼23% survived in the Au-LTO NS system. Furthermore, the concentration of the trapped electrons (900−1000 nm) reduced faster than that of the free electrons (1000−1200 nm). A similar phenomenon has been observed in the Au/TiO_2 system,[29] which implied a fast charge recombination between the trapped electrons in semiconductors and the holes in Au before diffusing away from the vicinity of the Au particles. To study the decay kinetics of trapped electrons, the time profiles of absorption probed at 925 nm were fitted using a multiexponential function as shown in Figure 6c. The lifetimes (τ_i) and amplitudes (a_i) are presented in Table 1. The transient absorption trace on the Au-LTO NSP was fitted to a three-exponential function with time constants of 4.8 (23%), 227 (20%), and 2800 ps (57%). Three decay lifetimes for Au-LTO NS were also obtained: 4.2 (22%), 250 (29%), and 1100 ps (49%). As illustrated in Figure 6d, the three time scales represent three different electron decay processes in the Au-LTO systems. The shortest component (τ_1) corresponded to the recombination of LSPR modes of Au NRs, namely, the hot electron relaxation process within Au. It has been reported that the apparent lifetime of the hot electron−hole recombination in bare Au NRs at the LSPR band was several picoseconds.[24] Hot electrons transfer from Au to LTO, competitive with SPR modes for recombination, resulted in the quenching of SPR PL.[27] The proportions of the transferred hot electrons (injection efficiency, $1 - a_1$) in Au-LTO NSP (77%) and Au-LTO NS (78%) systems were very similar, indicating that the geometry of the LTO substrate had little effect on the formation of Schottky barriers between Au and LTO. The second component with a lifetime of several hundreds of picoseconds (τ_2) was due to the electrons injected from Au into the neighboring (010) and/or (012) facets of LTO NSP (or the neighboring (010) facets of LTO NS) within a short distance. Lacking effective diffusion, 20% of the trapped electrons in LTO NSP (or 29% of the trapped electrons in LTO NS) rapidly recombined with the holes in Au in 200−300 ps. The relatively long-lived component, τ_3, could be attributed to the recombination between the long-distance diffused electrons in LTO and the holes in Au. The larger the τ_3 is, the lower probability for electron−hole pairs recombination, while in turn the redox reaction can take place more easily. Therefore, the τ_3 of Au-LTO NSP (2800 ps), which was much longer than that of Au-LTO NS (1100 ps), clearly demonstrated the more efficient charge carrier separation process in the Au-LTO NSP system. Note that, comparing with Au-LTO NS, Au-LTO NSP also revealed an increased a_3 value. Because the exposed (010) facets had more negative CBM potential (−0.72 eV vs NHE) than (012) facets (−0.52 eV vs NHE) within a LTO NSP particle,[34] the match of work functions of Au with (010) facets was higher than those of Au with (012) facets. A large proportion of photogenerated electrons preferentially injected from Au into (010) facets, while a small part of electrons injected from Au into (012) facets nearby. However, because of the built-in field established by successive surface heterojunctions, the injected electrons in (010) surfaces readily transferred to adjacent (012) surfaces

Table 1. Lifetimes (τ_i) and Amplitudes (a_i) of the Transient Absorption Decays for Au-LTO Samples

sample	τ_1 (a_1)	τ_2 (a_2)	τ_3 (a_3)
Au-LTO NSP	4.8 ± 0.7 ps (23%)	230 ± 50 ps (20%)	2800 ± 900 ps (57%)
Au-LTO NS	4.2 ± 0.4 ps (22%)	250 ± 30 ps (29%)	1100 ± 400 ps (49%)

DOI: 10.1021/acscatal.7b02972
ACS Catal. 2018, 8, 122−131

which were far away from Au NRs. The formed anisotropic electron flows from (010) to (012) surfaces thus increased the population of long-lived electrons and retarded the charge recombination process. As a result, the photocatalytic activity of the Au-LTO NSP system in the NIR region could be intensively improved.

CONCLUSIONS

In this work, Au NRs photosensitized LTO NSP hybrid structure was constructed and used as an efficient visible and NIR photocatalyst for H_2 evolution. The optimal H_2 evolution rate of Au-LTO NSP was 0.34 mmol g^{-1} h^{-1} under vis−NIR (λ > 420 nm) light irradiation, which was 2.4 and 4.7 times that of Au-LTO NS and Au-P25, respectively. The high AEQ of 1.4% at 920 nm irradiation indicated that the Au-LTO NSP composites could utilize NIR light efficiently. Single-particle fluorescence measurements showed that only the LSPR mode of Au NR realizes hot electron transfer to LTO NSP. Charge carrier lifetimes of Au-LTO NSP and Au-LTO NS measured by femtosecond TDR spectroscopy indicated that the redox reaction could take place more easily and the population of long-lived electrons was also greatly increased in the Au-LTO NSP system than in the Au-LTO NS system. Compared to LTO NS with only (010) facets exposure, a great part of injected hot electrons from Au NRs into the (010) facets of LTO NSP could efficiently migrate to the adjacent (012) facets and then be temporally stored there for further reactions, driven by successive surface heterojunctions. This is the first example to show the powerful role of a semiconductor surface heterojunction in favoring the plasmon-induced interfacial hot electron transfer.

EXPERIMENTAL SECTION

Preparation of $La_2Ti_2O_7$ Nanostructures. LTO nanosteps and nanosheets were respectively synthesized by the molten-salt method and the hydrothermal method, following our previous publications.[34,37]

Preparation of Au Nanorods. A seed-mediated method was employed to synthesize Au NRs.[46] First, a freshly prepared, ice-cold $NaBH_4$ (Fluka, 0.6 mL, 0.01 M) aqueous solution was instantly added into the CTAB (TCI, 5 mL, 0.2 M) and $HAuCl_4{\cdot}3H_2O$ (Sigma-Aldrich, 5 mL, 0.5 mM) mixture solution. A seed solution was obtained by vigorously stirring the above solution for 2 min and then aging at 30 °C for 2 h. Second, 3.6 g of CTAB and 0.493 g of sodium oleate (Tokyo Chemical Industry Co.) were dissolved in 100 mL of warm water (Millipore, 50 °C). Then 4 mL of a 4 mM $AgNO_3$ solution (Sigma-Aldrich) was added when the solution temperature was decreased to 30 °C. After gentle stirring (100 rpm) for 15 min, 100 mL of a $HAuCl_4{\cdot}3H_2O$ solution (1 mM) was added. Upon 90 min of stirring at 700 rpm, 0.6 mL of HCl (37 wt % in water, Wako) was then introduced, followed by another 15 min of slow stirring (400 rpm). By adding 0.32 mL of 0.064 M ascorbic acid (Sigma-Aldrich) and vigorous stirring for 30 s, the growth solution was prepared. Finally, 0.04 mL of seed solution was injected to the entire growth solution. After stirring for 30 s, the mixture was left undisturbed at 30 °C for 12 h. The final product of 860-Au NRs was isolated by centrifugation at 7000 rpm for 30 min to remove the supernatant.

Preparation of Au-LTO Composites. A ligand-exchange method was used to deposit Au NRs on LTO nanostructures to obtain the Au-LTO hybrid structures.[35] A total of 100 mg of LTO was dispersed in 100 mL of aqueous solution containing 100 μL of $NH_3{\cdot}H_2O$ (28%, Nacalai Tesque) and 100 μL of 3-mercaptopropionic acid (MPA, Sigma-Aldrich) for 12 h. Then, a calculated volume of Au NRs solution (concentration determined by ICP measurements) was introduced. After sufficient stirring for 12 h, the mixture was centrifuged, washed with water and ethanol, dried at 60 °C for 12 h, and annealed at 200 °C for 2 h to obtain the final product.

Characterization of Materials. XRD (Rigaku, Smartlab; operated at 40 kV and 200 mA, Cu Kα source) was employed to examine the structures of the samples. SEM (JEOL, JSM-6330FT) and TEM (JEOL, JEM3000F operated at 300 kV or Hitachi, H-800 operated at 200 kV) equipped with an EDS analyzer were used to investigate the morphologies, microstructures, and compositions. The XPS measurements were carried out on a PHI X-tool 8ULVAC-PHI instrument. The steady-state absorption and diffuse reflectance spectra were conducted on a UV−vis−NIR spectrophotometer (Jasco, V-770) at room temperature.

Photocatalytic H_2 Evolution. A total of 10 mg of photocatalyst was dispersed in 10 mL of aqueous solution containing 20 vol % methanol (Nacalai Tesque) in a 30 mL glass tube. Prior to the irradiation, the tube was sealed with a rubber septum and then bubbled with Ar gas for 20 min to completely remove the oxygen. The sample was irradiated using a Xe lamp (Asahi Spectra, HAL-320; 350 mW cm^{-2}) with constant stirring at room temperature. The volume of the generated H_2 was measured using a gas chromatograph (Shimadzu GC-8A). The AQE was calculated as AQE = (2 × number of evolved H_2 molecules/number of incident photons) × 100%.

Photoelectrochemical Measurements. Photoelectrochemical (PEC) measurements were conducted in three-electrode quartz cells connected with an electrochemical analyzer (ALS, model 660A). A platinum wire and Ag/AgCl electrode were used as the counter electrode and reference electrode, respectively. Au-LTO NSP, Au-LTO NS, and Au-P25 film electrode on an ITO substrate (BAS Inc., ITO11) served as the working electrode. A 0.1 M Na_2SO_4 aqueous solution was used as the electrolyte. The photocurrent and EIS plots were obtained under a bias of 1.23 V vs reversible hydrogen electrode (RHE).

Single-Particle Photoluminescence Measurements. For the single-particle PL measurement, we use an objective scanning confocal fluorescence microscope (PicoQuant, MicroTime 200) to record the images and spectra. It was coupled with an oil-immersion objective lens (Olympus, UplanSApochromat, 100×, 1.4 NA). The circular-polarized 488 nm pulse wave laser source was controlled using a PDL-800B driver (PicoQuant). To excite Au NRs, the excitation power was 300 μW. A single-photon avalanche photodiode (Micro Photon Devices, PDM 50CT) was tuned using the dichroic beam splitter (Chroma, 405/488rdc) together with a long pass filter (Chroma, HQ513CP). The emission from the sample was collected and detected using the above objective and the photodiode, respectively. The imaging spectrograph (Acton Research, SP-2356) only receives the emission passing through a slit that entered on it. The spectrograph was equipped with EMCCD camera (Princeton Instruments, ProEM). Every spectrum was integrated for 20 s.

Time-Resolved Diffuse Reflectance Spectral Measurements. The femtosecond TDR spectra were measured by the

DOI: 10.1021/acscatal.7b02972
ACS Catal. 2018, 8, 122−131

pump and probe method. The source is a regeneratively amplified titanium sapphire laser (Spectra-Physics, Spitfire Pro F, 1 kHz), which is pumped using the Nd:YLF laser (Spectra-Physics, Empower 15). A titanium sapphire laser (Spectra-Physics, Mai Tai VFSJW; fwhm 80 fs) was used to generate the seed pulse. The excitation pulse (320 or 420 nm, 3 mJ pulse^{-1}) was from the optical parametric amplifier (Spectra-Physics, OPA-800CF-1). A white light continuum pulse was divided into two parts to serve as probe and reference lights. Laser fluctuation was compensated using the reference light. The sample powder was coated on a glass sheet. Both the probe and the reference lights were directed to the samples. A linear InGaAs array detector which was equipped with a polychromator (Solar, MS3504) was used to detect the reflected lights. The mechanical chopper which was synchronized to the laser repetition rate was used to chop the pump pulse. A pair of spectra were achieved with and without the pump. The absorption change (% absorption) induced by the pump pulse was estimated based on these two spectra.

■ ASSOCIATED CONTENT

Supporting Information

The Supporting Information is available free of charge on the ACS Publications website at DOI: 10.1021/acscatal.7b02972.

vis−NIR absorption spectra and TEM images, Figure S1; structural parameters, Table S1; STEM-EDS images, Figure S2; EDS, Figure S3; XRD patterns, Figure S4; XPS, Figure S5; irradiance spectrum, Figure S6; photocatalytic H_2 evolution, Figures S7, S8, and S12; XRD patterns, SEM image, TEM image, and UV−vis−NIR DRS, Figures S9−S11; photocurrents and EIS plots, Figure S13; SEM images, Figure S14; single-particle PL spectra, Figures S15 and S16; statistical graph of PL intensity, Figure S17. (PDF)

■ AUTHOR INFORMATION

Corresponding Authors

*E-mail: zjy@buaa.edu.cn.

*E-mail: majima@sanken.osaka-u.ac.jp.

ORCID

Mingshan Zhu: 0000-0002-5926-5383

Mamoru Fujitsuka: 0000-0002-2336-4355

Junying Zhang: 0000-0002-4860-8774

Tetsuro Majima: 0000-0003-1805-1677

Notes

The authors declare no competing financial interest.

■ ACKNOWLEDGMENTS

This project is financially supported by National Natural Science Foundation of China (Nos. 51472013 and 51672106) and the Excellence Foundation of BUAA for PhD Students (No. 2017061). We thank the help from the Comprehensive Analysis Center of SANKEN, Osaka University. This work is partly supported by a Grant-in-Aid for Scientific Research (Project 25220806 and others) from the Ministry of Education, Culture, Sports, Science and Technology (MEXT) of the Japanese Government.

■ REFERENCES

(1) Chen, X.; Shen, S.; Guo, L.; Mao, S. S. *Chem. Rev.* **2010**, *110*, 6503−6570.

(2) Fujishima, A.; Honda, K. *Nature* **1972**, *238*, 37−38.

(3) Hisatomi, T.; Kubota, J.; Domen, K. *Chem. Soc. Rev.* **2014**, *43*, 7520−7535.

(4) Ismail, A. A.; Bahnemann, D. W. *Sol. Energy Mater. Sol. Cells* **2014**, *128*, 85−101.

(5) Wang, X.; Wang, F.; Sang, Y.; Liu, H. *Adv. Energy Mater.* **2017**, 1700473.

(6) Kou, J.; Lu, C.; Wang, J.; Chen, Y.; Xu, Z.; Varma, R. S. *Chem. Rev.* **2017**, *117*, 1445−1514.

(7) Li, Y.; Wang, Z.; Xia, T.; Ju, H.; Zhang, K.; Long, R.; Xu, Q.; Wang, C.; Song, L.; Zhu, J.; Jiang, J.; Xiong, Y. *Adv. Mater.* **2016**, *28*, 6959−6965.

(8) Sang, Y.; Zhao, Z.; Zhao, M.; Hao, P.; Leng, Y.; Liu, H. *Adv. Mater.* **2015**, *27*, 363−369.

(9) Chen, X.; Liu, L.; Yu, P. Y.; Mao, S. S. *Science* **2011**, *331*, 746−750.

(10) Hu, Y. H. *Angew. Chem., Int. Ed.* **2012**, *51*, 12410−12412.

(11) Chen, X.; Liu, L.; Huang, F. *Chem. Soc. Rev.* **2015**, *44*, 1861−1885.

(12) Li, Z. X.; Shi, F. B.; Zhang, T.; Wu, H. S.; Sun, L. D.; Yan, C. H. *Chem. Commun.* **2011**, *47*, 8109−8111.

(13) Guo, X.; Song, W.; Chen, C.; Di, W.; Qin, W. *Phys. Chem. Chem. Phys.* **2013**, *15*, 14681−14688.

(14) Tang, Y.; Di, W.; Zhai, X.; Yang, R.; Qin, W. *ACS Catal.* **2013**, *3*, 405−412.

(15) Meng, X.; Liu, L.; Ouyang, S.; Xu, H.; Wang, D.; Zhao, N.; Ye, J. *Adv. Mater.* **2016**, *28*, 6781−6803.

(16) Cushing, S. K.; Wu, N. *J. Phys. Chem. Lett.* **2016**, *7*, 666−675.

(17) Linic, S.; Christopher, P.; Ingram, D. B. *Nat. Mater.* **2011**, *10*, 911−921.

(18) Liu, L.; Ouyang, S.; Ye, J. *Angew. Chem., Int. Ed.* **2013**, *52*, 6689−6693.

(19) Zheng, Z.; Tachikawa, T.; Majima, T. *J. Am. Chem. Soc.* **2014**, *136*, 6870−6873.

(20) Elbanna, O.; Kim, S.; Fujitsuka, M.; Majima, T. *Nano Energy* **2017**, *35*, 1−8.

(21) Ng, C.; Cadusch, J. J.; Dligatch, S.; Roberts, A.; Davis, T. J.; Mulvaney, P.; Gomez, D. E. *ACS Nano* **2016**, *10*, 4704−4711.

(22) Su, R.; Tiruvalam, R.; Logsdail, A. J.; He, Q.; Downing, C. A.; Jensen, M. T.; Dimitratos, N.; Kesavan, L.; Wells, P. P.; Bechstein, R.; et al. *ACS Nano* **2014**, *8*, 3490−3497.

(23) Han, C.; Quan, Q.; Chen, H. M.; Sun, Y.; Xu, Y. J. *Small* **2017**, *13*, 1602947.

(24) Zhang, P.; Fujitsuka, M.; Majima, T. *Nanoscale* **2017**, *9*, 1520−1526.

(25) Pu, Y. C.; Wang, G.; Chang, K. D.; Ling, Y.; Lin, Y. K.; Fitzmorris, B. C.; Liu, C. M.; Lu, X.; Tong, Y.; Zhang, J. Z.; Hsu, Y. J.; Li, Y. *Nano Lett.* **2013**, *13*, 3817−3823.

(26) Jiang, W.; Bai, S.; Wang, L.; Wang, X.; Yang, L.; Li, Y.; Liu, D.; Wang, X.; Li, Z.; Jiang, J.; Xiong, Y. *Small* **2016**, *12*, 1640−1648.

(27) Lou, Z.; Fujitsuka, M.; Majima, T. *J. Phys. Chem. Lett.* **2017**, *8*, 844−849.

(28) Gołąbiewska, A.; Malankowska, A.; Jarek, M.; Lisowski, W.; Nowaczyk, G.; Jurga, S.; Zaleska-Medynska, A. *Appl. Catal., B* **2016**, *196*, 27−40.

(29) Bian, Z.; Tachikawa, T.; Zhang, P.; Fujitsuka, M.; Majima, T. *J. Am. Chem. Soc.* **2014**, *136*, 458−465.

(30) Liu, X.; Iocozzia, J.; Wang, Y.; Cui, X.; Chen, Y.; Zhao, S.; Li, Z.; Lin, Z. *Energy Environ. Sci.* **2017**, *10*, 402−434.

(31) Wu, B.; Liu, D.; Mubeen, S.; Chuong, T. T.; Moskovits, M.; Stucky, G. D. *J. Am. Chem. Soc.* **2016**, *138*, 1114−1117.

(32) Hong, J. W.; Wi, D. H.; Lee, S. U.; Han, S. W. *J. Am. Chem. Soc.* **2016**, *138*, 15766−15773.

(33) Wang, L.; Ge, J.; Wang, A.; Deng, M.; Wang, X.; Bai, S.; Li, R.; Jiang, J.; Zhang, Q.; Luo, Y.; Xiong, Y. *Angew. Chem.* **2014**, *126*, 5207−5211.

(34) Cai, X.; Mao, L.; Zhang, J.; Zhu, M.; Fujitsuka, M.; Majima, T. *J. Mater. Chem. A* **2017**, *5*, 10442−10449.

DOI: 10.1021/acscatal.7b02972
ACS Catal. 2018, 8, 122−131

(35) Ding, D.; Liu, K.; He, S.; Gao, C.; Yin, Y. *Nano Lett.* **2014**, *14*, 6731−6736.
(36) Chastain, J.; King, R. C.; Moulder, J. *Handbook of X-ray photoelectron spectroscopy: a reference book of standard spectra for identification and interpretation of XPS data*; Physical Electronics Division, Perkin-Elmer Corporation: Eden Prairie, MN, 1992.
(37) Cai, X.; Zhang, J.; Fujitsuka, M.; Majima, T. *Appl. Catal., B* **2017**, *202*, 191−198.
(38) Zhu, M.; Cai, X.; Fujitsuka, M.; Zhang, J.; Majima, T. *Angew. Chem., Int. Ed.* **2017**, *56*, 2064−2068.
(39) Ma, L.; Liang, S.; Liu, X.-L.; Yang, D.-J.; Zhou, L.; Wang, Q.-Q. *Adv. Funct. Mater.* **2015**, *25*, 898−904.
(40) Primo, A.; Corma, A.; García, H. *Phys. Chem. Chem. Phys.* **2011**, *13*, 886−910.
(41) Gomes Silva, C.; Juárez, R.; Marino, T.; Molinari, R.; García, H. *J. Am. Chem. Soc.* **2011**, *133*, 595−602.
(42) Zheng, Z.; Tachikawa, T.; Majima, T. *Chem. Commun.* **2015**, *51*, 14373−14376.
(43) Wackenhut, F.; Failla, A. V.; Meixner, A. J. *J. Phys. Chem. C* **2013**, *117*, 17870−17877.
(44) Bian, Z.; Tachikawa, T.; Kim, W.; Choi, W.; Majima, T. *J. Phys. Chem. C* **2012**, *116*, 25444−25453.
(45) Yoshihara, T.; Katoh, R.; Furube, A.; Tamaki, Y.; Murai, M.; Hara, K.; Murata, S.; Arakawa, H.; Tachiya, M. *J. Phys. Chem. B* **2004**, *108*, 3817−3823.
(46) Ye, X.; Zheng, C.; Chen, J.; Gao, Y.; Murray, C. B. *Nano Lett.* **2013**, *13*, 765−771.

DOI: 10.1021/acscatal.7b02972
ACS Catal. 2018, 8, 122−131